RSC Advances

ROYAL SOCIETY OF CHEMISTRY

www.rsc.org/advances

Facile synthesis of multifunctional $La_{1-x}Sr_xMnO_3$@Au core-shell nanoparticles for biomedical application

Xiao Liu[1], Hong-Ling Liu[1*], Ning Fang[1], Xue-Mei Li[1], Wei-Hua Guo[2], Jun-Hua Wu[3*], Mei-Xia Zhao[4*]

1 Institute of Molecular and Crystal Engineering, School of Chemistry and Chemical Engineering, Henan University, Kaifeng 475001, China

Email address: hlliu@henu.edu.cn

2 College of Life Science, Shandong University, Jinan 250100, China

3 Pioneer Research Center for Biomedical Nanocrystals, Korea University, Seoul 136-713, South Korea

Email address: wjhtsinghua@163.com

4 Key Laboratory of Natural Medicine and Immune Engineering, Henan University, Kaifeng 475001, China

Email address: zhaomeixia2011@henu.edu.cn

Abstract:

Multifunctional high-performance $La_{1-x}Sr_xMnO_3$@Au core-shell nanoparticles were successfully synthesized by a modified nanoemulsion method with the assistance of poly(ethylene glycol)-block-poly(propylene glycol)-block-poly(ethylene glycol) (PEO-PPO-PEO). The X-ray diffraction (XRD) and transmission electron microscopy (TEM) analyses confirm the structure and morphology of the nanoparticles. The measurements performed by ultraviolet-visible light absorbance spectrometry (UV-vis), vibrating sample magnetometry (VSM), and physical property measurement system (PPMS) demonstrate that the nanoparticles exhibit a surface plasmon resonance (SPR) absorption band around 561 nm from nanostructured Au and unique

magnetic nature at room temperature. Particularly, a sharp, tight phase transition from ferromagnetic to superparamagnetic states is observed in a free-standing $La_{1-x}Sr_xMnO_3$ nanoparticle system for the first time with a Curie temperature around room temperature. The cytotoxicity of the nanoparticles was studied for safe biomedical applications by MTT assay. The results show that the $La_{1-x}Sr_xMnO_3$@Au core-shell nanoparticles with lower cytotoxicity, well-defined magnetic and optical properties are promised for optical, magnetic, and biomedical application.

Keywords: $La_{1-x}Sr_xMnO_3$@Au; Optical-magnetic properties; Curie temperature; Biocompatibility

1. Introduction

Magnetic nanoparticles have received intense attention for biomedical applications including magnetic resonance imaging, magnetic hyperthermia treatment for malignant cells, targeted drug delivery, and magnetic cell separation due to their unique physicochemical properties at the nanoscale.[1-7] In particular, magnetic iron oxide including magnetite (Fe_3O_4) and maghemite (γ-Fe_2O_3) have been extensively studied in magnetic hyperthermia treatment, referring to the introduction of ferromagnetic or superparamagnetic particles into the tumor tissue in the way that the magnetic nanoparticles create heat that can be used to treat cancer when they are placed in alternating magnetic fields.[8,9] If the temperature reaches up to 43-45ºC, the cancer cells can be irreversibly destroyed while healthy tissues remain unaffected. Unfortunately, Fe_3O_4 and γ-Fe_2O_3 have a very high Curie temperature (T_c) ~823 K, which is

much higher than the hyperthermia temperature. The factor tremendously restricts their applications in magnetic hyperthermia therapy.[10-11] Currently, rare earth-based half-metallic ferromagnetic materials, such as the series of $La_{1-x}Sr_xMnO_3$ compounds, have attracted enormous awareness in the biomedical field especially for magnetic hyperthermia functioning due to their tunable transition temperature (T_c) from 283 to 370 K and have a large magnetic moment at room temperature.[12-15] In fact, the magnetic materials will provide more heating in the ferromagnetic state (below T_c), and vice versa, less heating in paramagnetic state (above T_c).[16] Hence, the preparation of $La_{1-x}Sr_xMnO_3$ compounds in the form of nanoparticles with a sharp, tight phase transition from ferromagnetic to superparamagnetic states around room temperature is hotly pursued. In our work, the resulting $La_{1-x}Sr_xMnO_3$@Au core-shell nanoparticles reveal superb magnetic behavior. Particularly, a sharp, narrow phase transition from ferromagnetic to superparamagnetic states is observed in a freestanding $La_{1-x}Sr_xMnO_3$ nanoparticle system for the first time with a Curie temperature around room temperature.

Although the distinctive physical properties of $La_{1-x}Sr_xMnO_3$ compounds make them highly suitable as effective heating materials for magnetic hyperthermia purposes, another prominent issue from the pointview of practical application in biomedicine is the biocompatibility of such a material. Many constructive approaches are recommended to triumph over the barriers in the way that new synthetic methods are proposed to obtain high-performance $La_{1-x}Sr_xMnO_3$ nanoparticles and then bare magnetic $La_{1-x}Sr_xMnO_3$ nanoparticles are modified with other bio-friendly materials, such as polymers, organic materials, and inorganic materials.[5,17-20] Among the various kinds of materials, gold as a well-studied

material because of its biological compatibility, catalytic activity, plasmonic property, and prevailing effects of surface plasmon resonance in the visible region, offers an excellent, versatile potential in immunoassay, biosensing, and optimal catalysis,[21-26] and we have synthesized gold coated Fe_3O_4 nanoparticles for successful cell separation.[27,28] Therefore, nano-engineering the two materials in the configuration of the $La_{1-x}Sr_xMnO_3$ nanoparticles covered with a thin gold shell, the ensuing core-shell nanostructure would not only provide all the characteristics of the gold and $La_{1-x}Sr_xMnO_3$ nanoparticles, but also protect core nanoparticles from corrosion and oxidation. Hence, gold coating over $La_{1-x}Sr_xMnO_3$ nanoparticle is an even more attractive composite system. In previous experimentation of preparing $La_{1-x}Sr_xMnO_3$ nanoparticles by different methods,[6,13,29-32] the convergent integration of gold with $La_{1-x}Sr_xMnO_3$ nanoparticles into composite nanostructures was attempted with encouraging outcomes, but more efforts are obviously required.[33-36]

As often nanoparticles as synthesized are of necessity to be processed and transferred to in an aqueous medium in applications of nanomedicine and nanobiotechnology, a bio-friendly, hydrophilic, and functionalizable surface is actively sought for biomedical uses and is usually achieved through a second step of surface modification. In our research, excellent core-shell nanoparticles could be synthesized via a well-established nanoemulsion method aided by poly(ethylene glycol)-block-poly(propylene glycol)-block-poly(ethylene glycol) (PEO-PPO-PEO). The triblock copolymer possesses many unique qualities, for instance, biocompatibility, non-charging, non-toxicity, and aqueous solubility, and is regularly

used in different fields.[37-41] In the nanoemulsion synthesis, the PEO-PPO-PEO molecules participate in the reactions primarily as a surfactant, besides playing the role of stabilizing the nanoparticles formed, and yet acting as a reducing agent. Adopting this methodology, we have prepared many long-term stable, monosized, highly crystalline nanoparticles, for instance, Fe_3O_4@ZnO, Fe_3O_4@Au, Au@Fe_3O_4 and Fe_3O_4-$Ca_3(PO_4)_2$.[27,28,42-44] In this work, the multifunctional, high-performance $La_{1-x}Sr_xMnO_3$@Au core-shell nanoparticles with PEO-PPO-PEO as the surfactant were successfully synthesized in three consecutive steps, which was based on well-established nanoemulsion method. The resulting nanoparticles are monosized and of high crystallinity, which reveal two kinds of well-shaped absorption bands, and superb magnetic behavior. In addition, the $La_{1-x}Sr_xMnO_3$@Au core-shell nanoparticles could be directly dispersed in both aqueous and organic media without further surface modification, bestowing the interesting amphiphility and show a sharp transition from ferromagnetic to superparamagnetic states for the first time in the isolated $La_{1-x}Sr_xMnO_3$ nanoparticles. The biocompatibility of the optimized $La_{1-x}Sr_xMnO_3$@Au core-shell nanoparticles against $La_{1-x}Sr_xMnO_3$ was evaluated on HepG2 cell by MTT assay. The outcomes prove that the $La_{1-x}Sr_xMnO_3$@Au nanoparticles have application potential in optical, magnetic, and biomedical fields.

2. Experimental

2.1. Materials

The major precursors used for the nanoemulsion synthesis of the $La_{1-x}Sr_xMnO_3$@Au core-shell nanoparticles are lanthanum (III) acetylacetonate ($La(acac)_3$, 99.9%), strontium (II) acetylacetonate ($Sr(acac)_2$, 99.9%), manganese (III) acetylacetonate ($Mn(acac)_3$, 99.9%), and gold acetate ($Au(ac)_3$, 99.9%). Other chemicals include triblock copolymer, poly(ethylene glycol)-block-poly(propylene glycol)-block-poly(ethylene glycol) (PEO-PPO-PEO, Mn=5800), 1,2-hexadecanediol ($C_{14}H_{29}CH(OH)CH_2(OH)$, 90%), octyl ether ($C_8H_{17}OC_8H_{17}$, 99%), and solvents such as hexane and ethanol. All materials were used as received without further processing.

2.2 Synthesis of $La_{1-x}Sr_xMnO_3$@Au core-shell nanoparticles

The $La_{1-x}Sr_xMnO_3$@Au core-shell nanoparticles were effectively synthesized by three consecutive steps. In the stage A, a typical experiment was carried out in a 100 ml flask, 1.3488 mmol (0.5884 g) of lanthanum (III) acetylacetonate, 0.4510 mmol (0.1289 g) of strontium (II) acetylacetonate, 1.7998 mmol (0.6340 g) of manganese (III) acetylacetonate, 0.4748 g of PEO-PPO-PEO as the surfactant, and 0.3881 g of 1,2-hexadecanediol were dissolved in 30 ml octyl ether under vigorous stirring. Subsequently, the reaction mixture was slowly heated to 120ºC within 2 h and homogenized for 2 h at 120ºC, then rapidly heated to 300ºC within 10 min and refluxed for 72 h at 300ºC. After cooling down to room temperature, the precipitated product was washed with mixed solvents of ethanol/hexane ($V_{ethanol/hexane}$ is 2:1) twice and a black powder was collected. In the stage B, the powder was annealed to 800ºC within 2 h and maintained for 12 h at 800ºC in a tube furnace. The product $La_{1-x}Sr_xMnO_3$ nanoparticles prepared via the stage A and B were separately stored for comparison. In the stage C, some desired amount of aqueous solution of $Au(OOCCH_3)_3$ (0.2667 g) was slowly added to the aqueous solution mixture of PEO-

PPO-PEO (0.5042 g) and $La_{1-x}Sr_xMnO_3$ nanoparticles (0.1069 g) under vigorous stirring. After the completion of the reaction, the resulting product was purified several times by magnetic separation to remove the solvent molecules and other residuals from the nanoparticles.

2.3. Structural characterization and measurements of the nanoparticles

The crystal structure of the synthesized $La_{1-x}Sr_xMnO_3$@Au core-shell nanoparticles was acquired by X-ray diffraction (XRD, Philips X'Pert Pro, Philips, Amsterdam, Netherlands; λ=1.54056Å) using Cu K_α radiation. TEM (JEM-2010) including the mode of high resolution (HRTEM), selected-area electron diffraction (SAED) and energy dispersive X-ray analysis (EDX) were used to characterize the morphologies, microstructure and elemental compositions. X-ray photoelectron spectroscopy (XPS) was carried out on a Thermo ESCALAB 250XI photoelectron spectrometer with Al K_α X-ray as the excitation source. The Fourier transform infrared spectroscopy studies of the $La_{1-x}Sr_xMnO_3$@Au core-shell nanoparticles and pure PEO-PPO-PEO polymer were performed using an Avatar 360 FTIR spectrometer (Nicolet Company, Madison, WI, USA). The optical and magnetic properties were subsequently investigated by a UV-vis (UV-vis near IR spectrophotometer, Hitachi U4100; Hitachi, Shanghai, China), VSM (Lakeshore 7300) and PPMS (Physical Property Measurement System, Quantum Design), respectively. The dispersion-collection processes of the $La_{1-x}Sr_xMnO_3$@Au core-shell nanoparticles both in water and hexane were visually demonstrated for application readiness.

2.4 Cytotoxicity study

2.4.1 Cell culture: The cytotoxicity of $La_{1-x}Sr_xMnO_3$ and $La_{1-x}Sr_xMnO_3$@Au core-shell nanoparticles was evaluated on HepG2 (human hepatocellular liver carcinoma)

cell. The HepG2 cells were cultured in RMPI-1640 medium supplemented with heat-inactivated FBS (10 % v/v) and 1% (v/v) penicillin-streptomycin (100 U/mL penicillin G and 100 mg mL^{-1} streptomycin) at 37°C under a 5% CO_2 atmosphere.

2.4.2 MTT assay: The HepG2 cells were seeded at a density of 5×10^4 cells/well in a 96-well microtire plate. After 24 h the old media was replaced by fresh media with different concentrations of $La_{1-x}Sr_xMnO_3$ and $La_{1-x}Sr_xMnO_3$@Au core-shell nanoparticles (20 and 100 μg/mL), respectively. Next, the total medium was incubated at 37ºC in a 5% CO_2 atmosphere for 48 h. After 48 h, the supernatant solution was removed and 20 μL MTT (2.5 mg/mL) solution was added into each test well and control wells as well. The plates were incubated for 4 h at 37ºC in a 5% CO_2 atmosphere for metabolization of MTT with the nanoparticles and cell media. Then, the medium was removed and the formed formazan was dissolved completely by adding 100 μL dimethyl sulfoxide (DMSO) solution. Finally, absorbance was read at 570 nm and the cell viability was accordingly calculated.

3. Results and discussion

3.1 Nanostructures and TEM morphology of $La_{1-x}Sr_xMnO_3$@Au core-shell nanoparticles

The morphology and particle size of the prepared $La_{1-x}Sr_xMnO_3$@Au core-shell nanoparticles were recorded by TEM. As shown in Fig. 1a, the $La_{1-x}Sr_xMnO_3$@Au nanoparticles are virtually uniform and nearly spherical in shape. The particle size histogram from the size counting of the nanoparticles garnered from a series of TEM images shows a tight size distribution, as shown in Fig. 1b, which is satisfactorily described by the curve of a Gaussian function and gives an average particle size of approximately 20.0 nm in diameter. As shown in Fig. 1c for a single nanoparticle, it is evident that the distinct fringe lattices run almost uniformly over the entire

nanoparticle, indicative of the single-crystallinity of the nanoparticle. As labeled, the spacing of 2.74 Å corresponds to the (104) reflection of the $La_{0.8}Sr_{0.2}MnO_3$ phase, whereas the lattices of the 2.04 Å spacing are assigned to the (200) reflection of the Au cubic phase. The observation clearly suggests the integration of both Au and $La_{1-x}Sr_xMnO_3$ compositions in the same nano-entity. The SAED result, as shown in Fig. 1d, gives a powder pattern, highlight the superposition of diffractions from scores of disoriented $La_{1-x}Sr_xMnO_3$@Au nanoparticles due to the size of the aperture. The sharpness and multiple diffraction spots observed in the pattern corroborate the high crystallinity of the monocrystalline $La_{1-x}Sr_xMnO_3$@Au nanoparticles. Fig. 1e further shows a typical TEM-EDX point-detection instance for the composition, undoubtedly confirming the simultaneous presence of La, Sr, Mn, O, and Au elements, and the atomic ratio of La/Sr in the $La_{1-x}Sr_xMnO_3$@Au core-shell nanoparticles has been estimated to be about 4.5, close to the initial input of the synthesis.

The nanoparticles were subsequently examined by X-ray crystal structural analysis. Fig. 2 represents the diffraction pattern obtained from the perovskite type crystalline structure of the synthesized $La_{1-x}Sr_xMnO_3$@Au core-shell nanoparticles, together with the perovskite type crystalline structure of $La_{0.8}Sr_{0.2}MnO_3$ (JCPDS card No. 53-0085), and cubic phased Au (JCPDS card No. 65-8601). The diffraction peaks of the $La_{1-x}Sr_xMnO_3$@Au core-shell nanoparticles may be indexed to two sets. The peaks positioning at 22.8º, 32.6º, 39.9º, 46.6º, 52.7º, 55.2º, 57.9º, and 68.4º (as labeled by the inverted triangles) are assigned to the (012), (104), (202), (024), (116), (008), (214) and (208) planes of the perovskite structure of $La_{0.8}Sr_{0.2}MnO_3$, whereas the peaks at 38.4º, 44.6º, 64.7º, 77.7º, and 81.9º (as labeled by the squares) are allocated to the (111), (200), (220), (311) and (222) planes of the Au cubic phase. The strong, well-defined, distinct peaks from the perovskite structure substantiate that the La_{1-}

$_xSr_xMnO_3$@Au core-shell nanoparticles are in a highly crystalline state. At the same time, based on the full width at half maximum (FWHM) of the most intense diffraction peaks by using the Debye-Scherrer equation, the average particle size of the $La_{1-x}Sr_xMnO_3$@Au core-shell nanoparticles is calculated to be ~18.7 nm, which comes close to the number from the statistical size counting of the TEM analysis above, supposing that the broadening of the peaks in the XRD pattern is predominantly due to the finite size effect of the nanoparticles.[45]

Fig. 3 shows a surveying XPS spectrum of the $La_{1-x}Sr_xMnO_3$@Au core-shell nanoparticles in the binding energy range of 0-900 eV and fingerprint scanning of the related individual metallic ions. The binding energies in the XPS spectra were calibrated using C 1s peak (285.2 eV). All indexed peaks are attributed to La, Sr, Mn, O, Au, and C, indicating the existence of relevant elements, as shown in Fig. 3a. The presence of carbon arises largely from the surfactant (PEO-PPO-PEO) molecules on the surface of the resulting nanoparticles. As a consequence, the nanoparticles are mostly composed of five elements, La, Sr, Mn, O, and Au. The La 3d core-level XPS spectrum of the $La_{1-x}Sr_xMnO_3$@Au core-shell nanoparticles is shown in Fig. 3b, with the binding energies of La $3d_{5/2}$ between 834.6 and 838.6 eV, and of La $3d_{3/2}$ between 851.5 and 855.5 eV, which confirm the existence of La^{3+} ions in the nanoparticles.[46] Fig. 3c shows Sr 3d XPS spectra, in which the two main peaks observed at the binding energy positions of 132.5 and 134.3 eV correspond to the Sr $3d_{5/2}$ and Sr $3d_{3/2}$, respectively, thus verifying the presence of Sr^{2+} in the sample.[46] The Mn 2p core-level XPS spectrum is shown in Fig. 3d for the $La_{1-x}Sr_xMnO_3$@Au core-shell nanoparticles. The peaks corresponding to the Mn $2p_{3/2}$ and Mn $2p_{1/2}$ core-levels were observed at 642.4 and 654.1 eV, respectively, bearing out the Mn composition. More precisely, the asymmetric peak of Mn $2p_{3/2}$ can be divided into two minor peaks by

Gaussian fitting: The Mn $2p_{3/2}$ features at 642.2 eV are attributed to oxides of Mn^{4+} and the peak position at 643.9 eV may be due to the manganese in different coordination environment from other metal ions such as La^{3+} and Sr^{2+}.[47] In addition, the binding energy at 84.3 and 87.9 eV, as shown in Fig. 3e, could be assigned to Au $4f_{7/2}$ and $4f_{5/2}$, respectively, indicating the Au metallic state.[48] The observation is in agreement with the XRD and TEM results as previously addressed. Moreover, the atomic ratio of La/Sr in the $La_{1-x}Sr_xMnO_3$@Au core-shell nanoparticles is assessed based on the XPS survey spectra to be about 4.9.

The validation of presence of the PEO-PPO-PEO macromolecules on the surface of the $La_{1-x}Sr_xMnO_3$@Au core-shell nanoparticles in this work was gathered by comparatively assessing the FTIR spectra of the pure PEO-PPO-PEO polymer and the $La_{1-x}Sr_xMnO_3$@Au core-shell nanoparticles after purification.[49-50] In Fig. 4a, the pure PEO-PPO-PEO molecules show one strong band at the position of ~1109.22 cm^{-1} due to the C-O-C stretching vibration of the ether bonding which commonly occurs in the range of 1250 cm^{-1} to 1000 cm^{-1} and one sharp band for the C-H bending vibration at the position of ~1465.7 cm^{-1}.[49-51] As displayed in Fig. 4b, these characteristic vibration and bending features persist in the FTIR spectrum of the PEO-PPO-PEO-laced $La_{1-x}Sr_xMnO_3$@Au core-shell nanoparticles, but red-shifting to the positions of 1064.35 cm^{-1} for the C-O-C stretching vibration and blue-shifting to the positions of 1633.57 cm^{-1} for the C-H bending vibration, correspondingly. The phenomenon may be caused by the interactive coordination of the oxygen atoms in the PEO-PPO-PEO main chains to the metal atoms in the hybrid nanostructure which could be attributed to changes in the elastic constants of bonding of the macromolecules sitting on the nanoparticle surface of high curvature as a result of the small nanoparticle size and interactions between the macromolecules and the nanoparticle surface.[49-50]

Furthermore, the characteristic band around 600 cm^{-1} observed in the $La_{1-x}Sr_xMnO_3$@Au samples corresponds to metal-oxygen bonds.[6,49] Consequently, the observation bestows robust evidence that the PEO-PPO-PEO molecules are covered onto the surface of the $La_{1-x}Sr_xMnO_3$@Au nanoparticles, since the superfluous PEO-PPO-PEO molecules were removed by the washing. Owing to the capping of the PEO-PPO-PEO macromolecules which have both hydrophilic and hydrophobic segments, thus the surface of the $La_{1-x}Sr_xMnO_3$@Au core-shell nanoparticles become amphiphilic, which enables a direct transfer of the nanoparticles to an aqueous medium without extra surface adornment.

3.2 Optical properties of $La_{1-x}Sr_xMnO_3$@Au core-shell nanoparticles

The optical properties of the PEO-PPO-PEO-laced $La_{1-x}Sr_xMnO_3$@Au core-shell nanoparticles were appraised by UV-visible absorption spectroscopy. It is well recognized that Au nanoparticles reveal an absorption band in the visible region arising from the surface plasmon resonance (SPR). Fig. 5 shows the UV-vis spectra of the $La_{1-x}Sr_xMnO_3$@Au nanoparticles separately dispersed in hexane (a), water (b), and ethanol (c), together with those of the $La_{1-x}Sr_xMnO_3$ nanoparticles in ethanol (d) and Au nanoparticles in hexane (e), in similar particle sizes. Obviously, the $La_{1-x}Sr_xMnO_3$@Au nanoparticles show two kinds of absorption bands, one from $La_{1-x}Sr_xMnO_3$ and the other from the SPR of the nanostructured Au. The strong absorption bands observed around 384 nm, 366 nm, and 374 nm for the spectra of the $La_{1-x}Sr_xMnO_3$@Au nanoparticles dispersed in hexane (Fig. 5a), water (Fig. 5b) and ethanol (Fig. 5c), respectively, are assigned to the absorption of the $La_{1-x}Sr_xMnO_3$ nanoparticles,[47] which correspond to blue-shifting from the absorption band of the $La_{1-x}Sr_xMnO_3$ nanoparticles in ethanol at the position of ~411 nm, as shown in Fig. 5d. The position of the surface plasmon band in the solution of the $La_{1-x}Sr_xMnO_3$@Au

nanoparticles varies from 564 nm in hexane, 546 nm in water, to 554 nm in ethanol, in comparison to an absorption peak at 528 nm from the Au nanoparticles in hexane, as shown in Fig. 5e.[52] The distinct red-shifting and broadening of the SPR of the $La_{1-x}Sr_xMnO_3$@Au core-shell nanoparticles relative to that of the Au nanoparticles is consistent with a previous report.[37] It is valuable to point out that the SPR band of metal nanoparticles strongly depends on the size, shape, composition, and dielectric property of the nanoparticles and the local environment.[27-28,42]

3.3 Magnetic properties of $La_{1-x}Sr_xMnO_3$@Au core-shell nanoparticles

The magnetic properties of the $La_{1-x}Sr_xMnO_3$ and $La_{1-x}Sr_xMnO_3$@Au core-shell nanoparticles were studied by VSM and PPMS. Fig. 6 are hysteresis loops, and field cooling (FC) and zero-field cooling (ZFC) curves of magnetization vs. temperatures (M-T) under an applied magnetic field of 500 Oe measured by PPMS on the sample, respectively. As Au and the PEO-PPO-PEO macromolecules are nonmagnetic in nature, thus the magnetism of the nanocomposite system comes dominantly from the core ingredient in the $La_{1-x}Sr_xMnO_3$@Au core-shell nanoparticles which is in turn protected by Au and PEO-PPO-PEO from oxidation. Fig. 6a shows the hysteresis curves of the $La_{1-x}Sr_xMnO_3$ and $La_{1-x}Sr_xMnO_3$@Au core-shell nanoparticles at 300 K. It is clear that the $La_{1-x}Sr_xMnO_3$@Au core-shell nanoparticles show superparamagnetic behavior with a small coercivity of ~9.0 Oe and lower magnetization of ~18.28 emu/g, while the $La_{1-x}Sr_xMnO_3$ nanoparticles was soft ferromagnetic or near superparamagnetic with a coercivity of ~15.2 Oe and magnetization of ~36.31 emu/g at room temperature. Compared to the $La_{1-x}Sr_xMnO_3$ nanoparticles, the $La_{1-x}Sr_xMnO_3$@Au core-shell nanoparticles are easier to saturate, which could be partly owing to proximity effects and unique spatial configurations.[28] The hysteresis curves for the $La_{1-x}Sr_xMnO_3$@Au core-shell nanoparticles at 5 K, 300

K, and 395 K are shown in Fig. 6b. The coercivity and magnetization decrease to ~0 Oe and ~2.52 emu/g at 395 K, and increase to ~69.39 Oe and ~30.09 emu/g at 5 K, separately. The magnetization increases with decreasing temperature owing to overcoming of the magnetic anisotropic energy over the thermal effect.[13,53]

Fig. 6c and 6d show the variation of magnetization (*M*) as a function of temperature (*T*) of the $La_{1-x}Sr_xMnO_3$ and $La_{1-x}Sr_xMnO_3$@Au core-shell nanoparticles in the range of 5 to 400 K in an external magnetic field of 500 Oe recorded in either zero-field-cooled (*ZFC*) or field-cooled (*FC*) mode, separately. As given in Fig. 6c, the $La_{1-x}Sr_xMnO_3$@Au core-shell nanoparticles show an initial increase from of ~0.17 emu/g at ~355 K to ~8.13 emu/g at ~320 K rapidly and again increase to the maximum of ~11.50 emu/g at ~140 K slowly and then gradual decrease to ~10.05 emu/g at ~5 K with decreasing temperature in the *FC* mode, in contrast to the *ZFC* mode which reveals likewise an initial increase from of ~0.16 emu/g at ~355 K to ~8.09 emu/g at ~320 K rapidly and again increase to the maximum of ~11.50 emu/g at ~140 K slowly, and then the magnetization almost keeps unchanged with decreasing temperature. The rapid change in magnetization over the narrow range of temperature is indicative of the ferromagnetic phase transition of the nanoparticle system. At the same time, we observed the same phenomenon in the $La_{1-x}Sr_xMnO_3$ sample, but the $La_{1-x}Sr_xMnO_3$@Au core-shell nanoparticles showed reduced saturation magnetization relative to $La_{1-x}Sr_xMnO_3$ due to reduction in the mass or volume fraction caused by the Au coating as expected.[54] Additionally, it is apparent that the merging of the *ZFC* and *FC* curves at the high temperatures is one of the

characteristic features of a superparamagnetic system and the phenomena as observed above clearly illustrate that the $La_{1-x}Sr_xMnO_3$@Au core-shell and $La_{1-x}Sr_xMnO_3$ nanoparticles possess the typical superparamagnetism of magnetic nanoparticles at high temperature, in addition to the sharp ferromagnetic phase transition.[13,14] The Curie temperature (T_c) of both the samples is determined from the maxima of the *dM/dT* versus *T* curve, as shown in the inset of Fig. 6c and 6d. The result shows that the T_c of the $La_{1-x}Sr_xMnO_3$@Au core-shell nanoparticles is evaluated to be ~328 K, which is less than that of the $La_{1-x}Sr_xMnO_3$ nanoparticles (338 K). Another important parameter is the blocking temperature (T_B), at which the magnetic anisotropy energy of a nanoparticle system is overcome by thermal energy and the whole system becomes superparamagnetic above T_B or magnetization of the particle is blocked below T_B.[13,55] T_B of the $La_{1-x}Sr_xMnO_3$@Au and $La_{1-x}Sr_xMnO_3$ nanoparticles is observed at the position of ~145 K and ~170 K, respectively. Compared to the $La_{1-x}Sr_xMnO_3$ nanoparticles, the decrease of T_C and T_B of the $La_{1-x}Sr_xMnO_3$@Au core-shell nanoparticles may be due to the particle size and the Au shell effect.[16,52] In our samples, no magnetic relaxation is observed below T_B, so the spin glass behavior does not exist and the system can be considered both the single domain and superparamagnetic in nature. Consequently, we have for the first time synthesized a free-standing $La_{1-x}Sr_xMnO_3$ nanoparticle system with a sharp, tight phase transition from ferromagnetic to superparamagnetic states.

As shown in Fig. 7, the $La_{1-x}Sr_xMnO_3$@Au core-shell nanoparticles in water, under the influence of an external magnetic field, change from a homogeneous, grey black dispersion (Fig. 7a) to a clear, transparent solution, with the nanoparticles collected by magnetic disc (Fig. 7b). The collected nanoparticles can be easily and reversibly dispersed by shaking-up after removal of the magnetic field and the above process can be repeated as many times as desired. A similar process happens to the nanoparticles in hexane, as shown in Fig. 7c and 7d. The color of the solution in Figure 7a and 7c is complementary to the corresponding UV-vis absorption of Fig. 5.

3.4 Cytotoxicity study

To examine the biocompatibility of $La_{1-x}Sr_xMnO_3$ and $La_{1-x}Sr_xMnO_3$@Au core-shell nanoparticles MTT assay is employed. MTT is a colorimetric cytotoxicity assay, which attempts to determine the mechanism behind the induced cell death. Mitochondrial activity can be tested by using tetrazolium salts (MTT), as mitochondrial dehydrogenase enzymes cleave the tetrazolium ring.[13-14] Since the reduction of MTT can only occur in metabolic active cells, the level of activity is a measure of the viability of the cells. The biocompatibility studies of both $La_{1-x}Sr_xMnO_3$ and $La_{1-x}Sr_xMnO_3$@Au core-shell nanoparticles have been evaluated on tumour cells with different concentrations by MTT assay. The tumour cells are incubated with the $La_{1-x}Sr_xMnO_3$@Au core-shell nanoparticles with different concentrations of 20 and 100 μg/mL at 37ºC in a 5% CO_2 atmosphere for 48 h. The relative cell viability (%) compared with the control well containing cells without

nanoparticles is calculated by the ratio of $[A]_{tested}/[A]_{control}\times100\%$. From the cytotoxicity data, it is found that there is a higher cytotoxicity observed in the $La_{1-x}Sr_xMnO_3$ nanoparticles sample, in contrast to the $La_{1-x}Sr_xMnO_3$@Au nanoparticles sample, as shown in Fig. 8.

4. Conclusions

We have succeeded in the facile synthesis of the PEO-PPO-PEO-laced, multifunctional high-performance $La_{1-x}Sr_xMnO_3$@Au core-shell nanoparticles by the modified nanoemulsion method using the triblock copolymer PEO-PPO-PEO as the surfactant. The morphology and structural analyses reveal the narrow particle size distribution with an average diameter ~20.0 nm and high crystallinity of the nanoparticles. The optical measurements present a well-defined absorption band of the nanoparticles which manifests the surface plasmon resonance (SPR) of the nanostructured Au. The magnetic characterization shows that we have for the first time prepared a free-standing $La_{1-x}Sr_xMnO_3$ nanoparticle with a sharp, narrow phase transition from ferromagnetic to superparamagnetic states. The cytotoxicity tests by MTT assaying reveal that the $La_{1-x}Sr_xMnO_3$@Au core-shell nanoparticles are more bio-friendly observed relative to the $La_{1-x}Sr_xMnO_3$ nanoparticles. Hence, the $La_{1-x}Sr_xMnO_3$@Au core-shell nanoparticles are promising for applications such as optical detection, magnetic separation and magnetic hyperthermia.

Acknowledgments

This work was supported in part by the National Natural Science Foundation of China (nos. 51172064, 31470402, 31270374 and U1204201), the National Research

Foundation of Korea (no. 2012-0005657, 2012-0001067), the Scientific and Technological Development Projects, Science and Technology Department of Henan Province, China, the Industrial Core Technology Development Program funded by the Ministry of Trade, Industry and Energy (no. 10033183), and the Seoul R&BD Program (no. 10920).

References

1 M. Kačenka, O. Kaman, J. Kotek, L. Falteisek, J. Černý, D. Jirák, V. Herynek, K. Zacharovová, Z. Berková, P. Jendelová, J. Kupčík, E. Pollert, P. Veverka, I. Lukeš, *J. Mater. Chem.*, 2011, **21**, 157-164.

2 S. Louguet, B. Rousseau, R. Epherre, N. Guidolin, G. Goglio, S. Mornet, E. Duguet, S. Lecommandoux, C. Schatz, *Polym. Chem.,* 2012, **3**, 1408-1417.

3 S. V. Jadhav, D. S. Nikam, V. M. Khot, N. D. Thorat, M. R. Phadatare, R. S. Ningthoujam, A. B. Salunkhe, S. H. Pawar, *New J. Chem*., 2013, **37**, 3121.

4 C. Kumar, F. Mohammad, *Adv. Drug Delivery Rev.,* 2011, **63**, 789-808.

5 K. R. Bhayani, S. N. Kale, S. Arora, R. Rajagopal, H. Mamgain, R. Kaul-Ghanekar, D. C. Kundaliya, S. D. Kulkarni, R. Pasricha, S. D. Dhole, S. B. Ogale, K. M. Paknikar, *Nanotechnology,* 2007, **18**, 345101.

6 N. D. Thorat, V. M. Khot, A. B. Salunkhe, A. I. Prasad, R. S. Ningthoujam, S. H. Pawar, *J. Phys. D: Appl. Phys.,* 2013, **46**, 105003.

7 S. Durdík, A. Krafcík, M. Babincová, P. Babinec, *Phys. Medica,* 2013, **29**, 562-567.

8 K. L. Ang, S. Venkatraman, R. V. Ramanujan, *Mater. Sci. Eng. C*., 2007, 27, 347-351.

9 A. K. Gupta, M. Gupta, *Biomaterials*., 2005, 26, 3995-4021.

10 E. Kita, T. Oda, T. Kayano, S. Sato, M. Minagawa, H. Yanagihara, M. Kishimoto, C. Mitsumata, S. Hashimoto, S. Yamada, N. Ohkohchi, *J. Phys. D: Appl. Phys.,*

2010, **43**, 474011.

11 C. J. Xu, S. H. Sun, *Adv. Drug Delivery Rev.,* 2013, **65**, 732-743.

12 P. B. Shete, R. M. Patil, N. D. Thorat, A. Prasad, R. S. Ningthoujam, S. J. Ghosh, S. H. Pawar, *Appl. Surf. Sci.,* 2014, **288**, 149-157.

13 N. D. Thorat, K. P. Shinde, S. H. Pawar, K. C. Barick, C. A. Betty, R. S. Ningthoujam, *Dalton Trans.,* 2012, **41**, 3060.

14 N. D. Thorat, R. M. Patil, V. M. Khot, A. B. Salunkhe, A. I. Prasad, K. C. Barick, R. S. Ningthoujam, S. H. Pawar, *New J. Chem.,* 2013, **37**, 2733-2742.

15 N. D. Thorat, S. V. Otari, R. A. Bohara, H. M. Yadav, V. M. Khot, A. B. Salunkhe, M. R. Phadatare, A. I. Prasad, R. S. Ningthoujam, S. H. Pawar, *Mater. Sci. Eng. C,* 2014, **42**, 637-646.

16 D. H. Manh, P. T. Phong, P. H. Nam, D. K. Tung, N. X. Phuc, I. J. Lee, *Physica B,* 2014, **444**, 94-102.

17 N. D. Thorat, V. M. Khot, A. B. Salunkhe, R. S. Ningthoujam, S. H. Pawar, *Colloids Surf. B: Biointerfaces,* 2013, **104**, 40-47.

18 F. J. Li, A. P. Zhu, X. L. Song, L. J. Ji, *Colloids Surf. B: Biointerfaces,* 2014, **115**, 377-383.

19 A. K. Pradhan, R. Bah, R. B. Konda, R. Mundle, H. Mustafa, *J. Appl. Phys.,* 2008, **103**, 07F704.

20 S. Brivio, C. Magen, A. A. Sidorenko, D. Petti, M. Cantoni, M. Finazzi, F. Ciccacci, R. D. Renzi, M. Varela, S. Picozzi, R. Bertacco, *Phys. Rev. B* 2010, **81**, 094410.

21 E. Boisselier, D. Astruc, *Chem. Soc. Rev.,* 2009, **38**, 1759-1782.

22 M. C. Daniel, D. Astruc, *Chem. Rev.,* 2004, **104**, 293-346.

23 T. Ogoshi, K. Umeda, T. A. Yamagishi, Y. Nakamoto, *Polymer J.,* 2008, **40**, 942-

943.

24 J. F. Hainfeld, R. D. Powell, *J. Histochem. Cytochem*., 2000, **48**, 471-480.

25 Y. X. Zhang, H. L. Ding, Y. Y. Liu, S. S. Pan, Y. Y. Luo, G. H. Li, *J. Mater. Chem*., 2012, 21, 10779-10786.

26 Z. C. Xu, Y. L. Hou, S. H. Sun, *J. Am. Chem. Soc*., 2007, 129, 8698-8699.

27 H. L. Liu, C. H. Sonn, J. H. Wu, K. M. Lee, Y. K. Kim, *Biomaterials,* 2008, **29**, 4003-4011.

28 H. L. Liu, J. H. Wu, J. H. Min, J. H. Lee, Y. K. Kim, *J. Nanosci. Nanotechnol.,* 2009, **9**, 754-758.

29 Y. L. Cheng, J. M. Dai, X. B. Zhu, D. J. Wu, Z. R. Yang, Y. P. Sun, *Nanoscale Res Lett*., 2009, 4, 1153-1158.

30 S. Daengsakul, C. Mongkolkachit, C. Thomas, S. Siri, I. Thomas, V. Amornkitbamrung, S. Maensiri, *Appl Phys A*., 2009, 96, 691-699.

31 M. Kačenka, O. Kaman, Z. Jirák, M. Maryško, P. Veverka, M. Veverka, S. Vratislav, *J. Solid State Chem*., 2015, 221, 364-372.

32 J. Hu, G. J. Shao, P Guo, X. J. Qin, G. Z. Xing, *Trans. Nonferrous Met. Soc. China*, 2008, 18, 351-355.

33 W. Wiyaratn, W. Appamana, S. Assabumrungrat, *J. Industrial Eng. Chem*., 2011, **17**, 474-478.

34 O. Pana, R. Turcu, M. L. Soran, C. Leostean, E. Gautron, C. Payen, O. Chauvet, *Synthetic Metals.,* 2010, **160**, 1692-1698.

35 O. Pana, R. Turcu, M. L. Soran, S. Macavei, C. Leostean, *J. Physics: Conference Series.,* 2009, **182**, 012071.

36 Y. X. Liu, H. X. Dai, J. G. Deng, X. W. Li, Y. Wang, H. Arandiyan, S. H. Xie, H. G. Yang, G. S. Guo, *J. Catalysis,* 2013, **305**, 146-153.

37 T. K. Jain, S. P. Foy, B. Erokwu, S. Dimitrijevic, C. A. Flask, V. Labhasetwar,

Biomaterials, 2009, **30**, 6748-56.

38 K. Hervè, L. Douziech-Eyrolles, E. Munnier, S. Cohen-Jonathan, M. Soucè, H. Marchais, P. Limelette, F. Warmont, M. L. Saboungi, P. Dubois, I. Chourpa, *Nanotechnology* 2008, **19**, 1-7.

39 J. P. Yang, Y. P. Zhai, Y. H. Deng, D. Gu, Q. Li, Q. L. Wu, Y. Huang, B. Tu, D. Y. Zhao, *J. Colloids Interface Sci.* 2010, **342**, 579-585.

40 F. Alexis, E. Pridgen, L. K. Molnar, O. C. Farokhzad, *Mol Pharm.,* 2008, **5**, 505-515.

41 S. Chen, Y. Li, C. Guo, J. Wang, J. H. Ma, X. F. Liang, L. R. Yang, H. Z. Liu, *Langmuir,* 2007, **23**, 1266976.

42 H. L. Liu, J. H. Wu, J. H. Min, X. Y. Zhang, Y. K. Kim, *Mater. Res. Bull.,* 2013, **48**, 551-558.

43 H. L. Liu, J. H. Wu, J. H. Min, Y. K. Kim, *J. Alloys Compounds,* 2012, **537**, 60-64.

44 H. L. Liu, J. H. Wu, J. H. Min, P. Hou, A. Y. Song, Y. K. Kim, *Nanotechnology,* 2011, **22**, 055701.

45 B. D. Cullity, S. R. Stock, Elements of X-ray Diffraction. New Jersey: Englewood Cliffs; 2001:167-171.

46 S. V. Jadhav, D. S. Nikam, V. M.Khot, S. S. Mali, C. K. Hong, S. H. Pawar, *Mater. Characterization,* 2015, **102**, 209-220.

47 A. Giri, N. Goswami, M. S. Bootharaju, P. L. Xavier, R. John, N. T. Thanh, T. Pradeep, B. Ghosh, A. K. Raychaudhuri, S. K. Pal, *J. Phys. Chem. C,* **2012**, *116*, 25623-25629.

48 Z. S. Hosseini, A. Mortezaali, A. Irajizad, S. Fardindoost, *J. Alloys Compounds,* 2015, **628**, 222-229.

49 X. H. Wang, X. Y. Zhang, W. Z. Cheng, H. Q. Shao, X. Liu, X. M. Li, H. L. Liu,

J. H. Wu, *Nanoscale Res. Lett.,* 2014, **9**, 1-7.

50 X. Liu, H. L. Liu, W. X. Zhang, X. M. Li, N. Fang, X. H. Wang, J. H. Wu, *Nanoscale Res. Lett.,* 2015, ***10***, 195.

51 C. Guo, H. Z. Liu, J. Y. Chen, *Colloid Polym. Sci.,* 1999, **277**, 376-381.

52 H. L. Liu, W. X. Zhang, P. Hou, J. H. Wu, *Gold Bull.,* 2011, **44**, 21-25.

53 G. Glöckl, R. Hergt, M. Weinberger, S. Dutz, S. Nagel, W. Weitschies, *J. Phys.: Condens. Matter,* 2006, **18**, S2935-S2949.

54 K. Zhang, T. Holloway, J. Pradhan, M. Bahoura, R. Bah, R. R. Rakhimov, A. K. Pradhan, R. Prabakaran, G. T. Ramesh, *J. Nanosci. Nanotechnol.,* 2010, **10**, 5520-5526.

55 A. Rostamnejadi, H. Salamati, P. Kameli, H. Ahmadvand, *J. Magn. Magn. Mater.,* 2009, **321**, 3126-3131.

Figure Captions

Fig. 1 TEM analyses of the $La_{1-x}Sr_xMnO_3$@Au core-shell nanoparticles. (a) Bright-field TEM image, (b) particle size distribution (in histogram) with Gaussian function fit (in curve), (c) HRTEM of an individual nanoparticle, (d) selected-area electron diffraction pattern of the sample, (e) point-detection EDX analysis.

Fig. 2 XRD diffraction analyses of the $La_{1-x}Sr_xMnO_3$@Au core-shell nanoparticles. Bar diagram for the JCPDS of $La_{0.8}Sr_{0.2}MnO_3$ (in inverted triangles), and Au (in squares)

Fig. 3 XPS spectra of the $La_{1-x}Sr_xMnO_3$@Au core-shell nanoparticles. (a) Surveying XPS spectrum, (b) La 3d spectrum, (c) Sr 3d spectrum, (d) Mn 2p spectrum, and (e) Au 4f spectrum.

Fig. 4 FTIR spectra of (a) the pure PEO-PPO-PEO polymer, and (b) the PEO-PPO-PEO-laced $La_{1-x}Sr_xMnO_3$@Au nanoparticles.

Fig. 5 UV-visible absorbance spectra of the PEO-PPO-PEO-laced $La_{1-x}Sr_xMnO_3$@Au nanoparticles dispersed in different solvents. Hexane (a), water (b), and ethanol (c), in comparison to $La_{1-x}Sr_xMnO_3$ nanoparticles in ethanol (d) and Au nanoparticles in hexane (e).

Fig. 6 Magnetic measurements of $La_{1-x}Sr_xMnO_3$@Au and $La_{1-x}Sr_xMnO_3$ nanoparticles. (a) Hysteresis curves for $La_{1-x}Sr_xMnO_3$@Au and $La_{1-x}Sr_xMnO_3$ at 300 K. (b) Hysteresis curves for $La_{1-x}Sr_xMnO_3$@Au at 5 K, 300 K, and 395 K. (c) FC and ZFC curves for $La_{1-x}Sr_xMnO_3$@Au under the magnetic field of 500 Oe. (d) FC and ZFC curves for $La_{1-x}Sr_xMnO_3$ under the magnetic field of 500 Oe.

Fig. 7 Photoimages of dispersion-collection processes of the $La_{1-x}Sr_xMnO_3$@Au core-shell nanoparticles. (a) Dispersion in water and corresponding magnetic collection (b), and (c) dispersion in hexane and corresponding magnetic collection (d).

Fig. 8 Cell viability data of the $La_{1-x}Sr_xMnO_3$@Au and $La_{1-x}Sr_xMnO_3$ nanoparticles by MTT assay on HepG2 cells for 48 h.

Table of Contents Graphic (TOC)

Multifunctional high-performance $La_{1-x}Sr_xMnO_3$@Au core-shell nanoparticles were synthesized by nanoemulsion process with the assistance of PEO. The nanoparticles show sharp, tight phase transition from ferromagnetic to superparamagnetic states, well dispersibility and excellent optical performance both in organic and aqueous solvent. At the same time, The cytotoxicity tests by MTT assaying reveal that the $La_{1-x}Sr_xMnO_3$@Au core-shell nanoparticles are more bio-friendly observed relative to the $La_{1-x}Sr_xMnO_3$ nanoparticles.

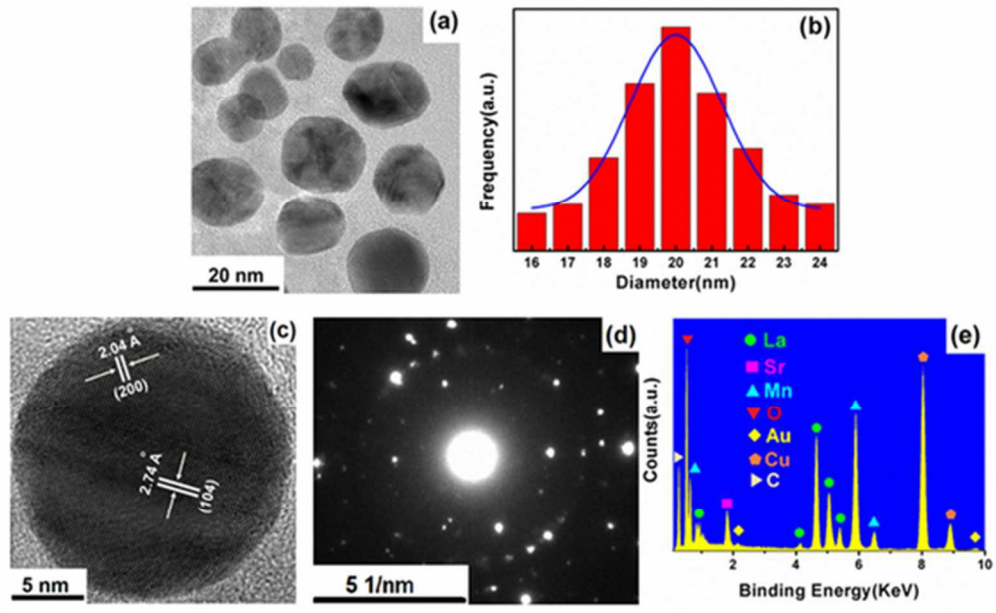

48x29mm (300 x 300 DPI)

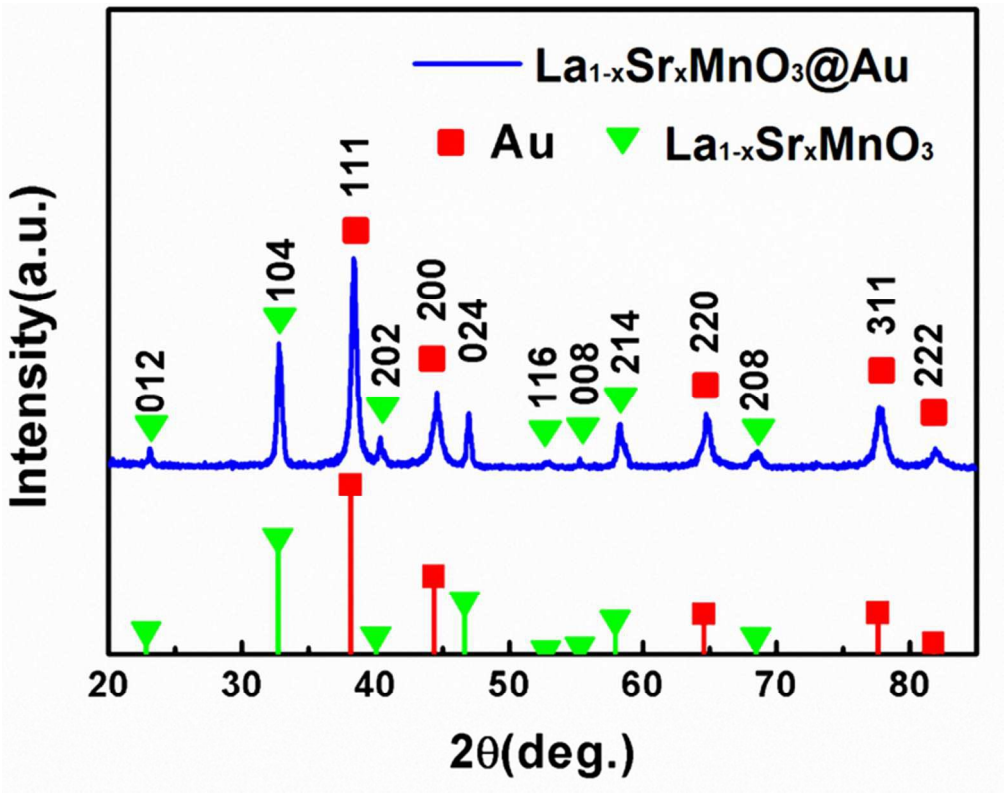

63x49mm (300 x 300 DPI)

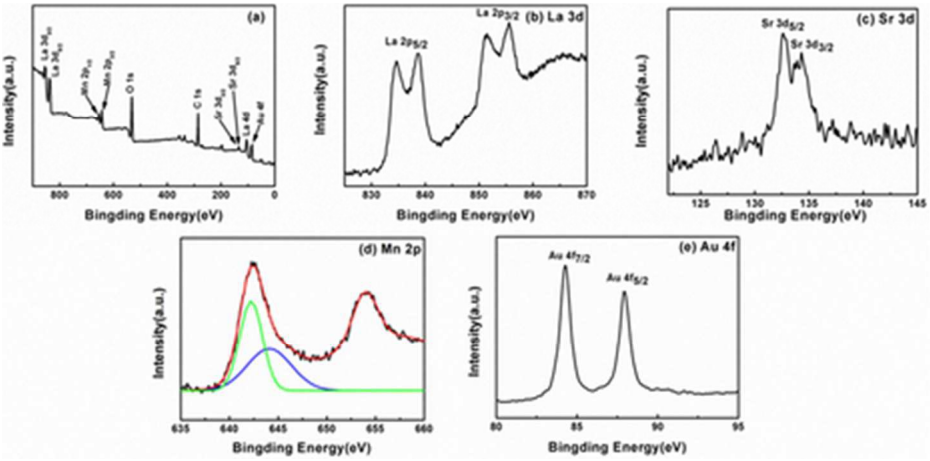

39x19mm (300 x 300 DPI)

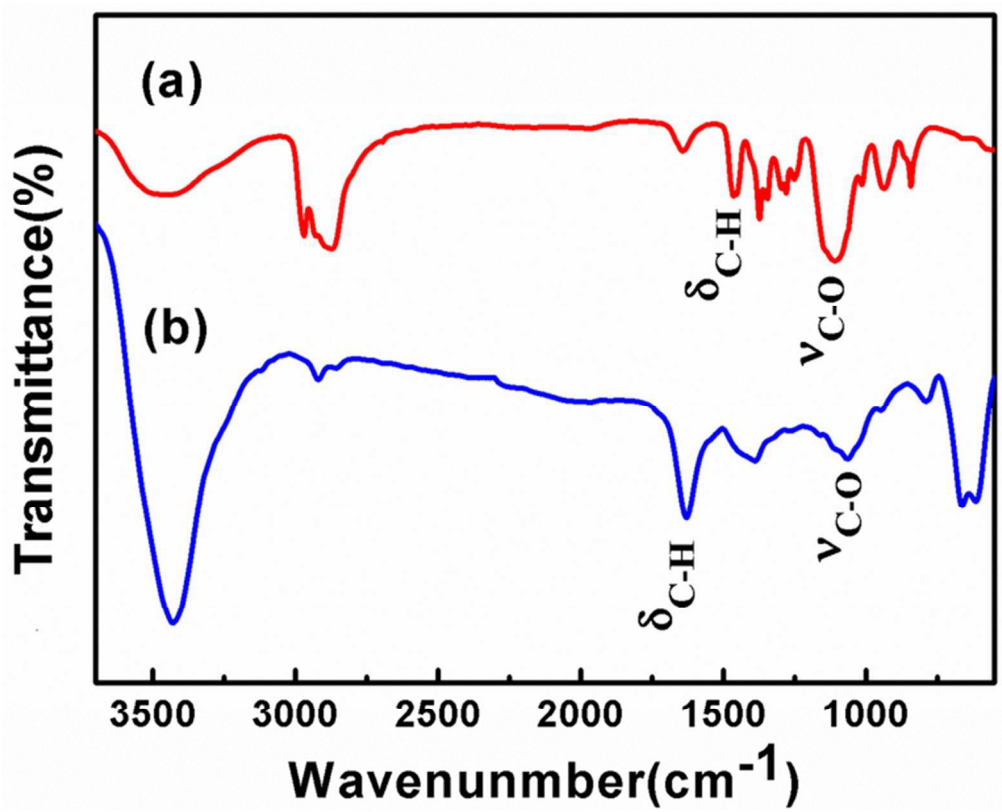

64x51mm (300 x 300 DPI)

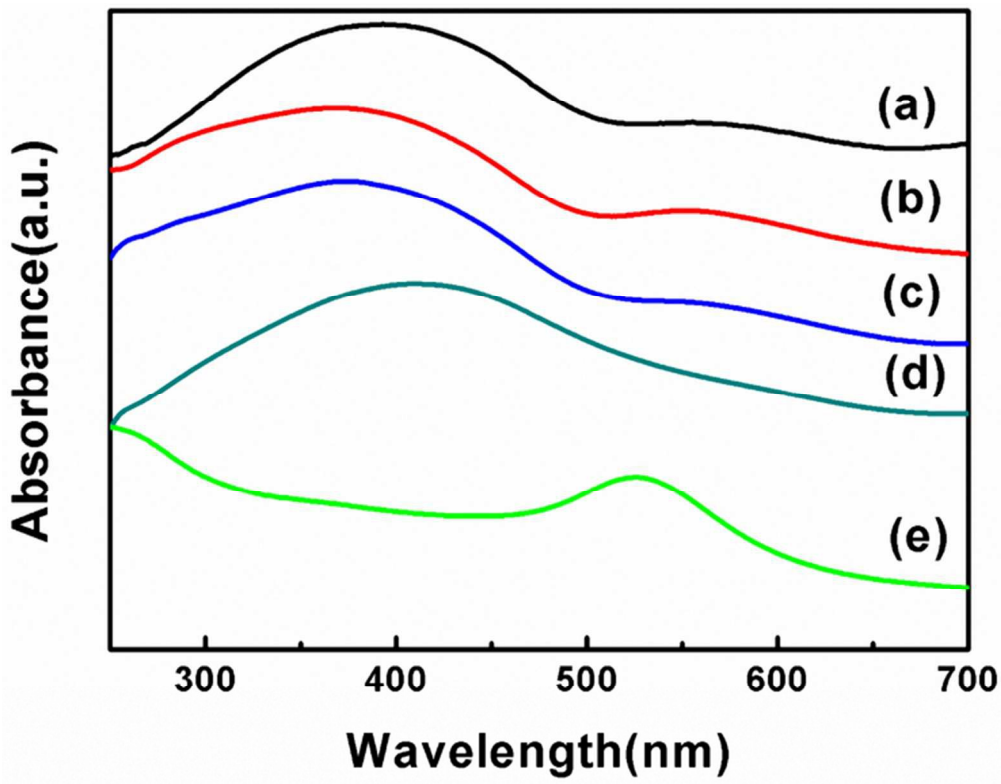

62x48mm (300 x 300 DPI)

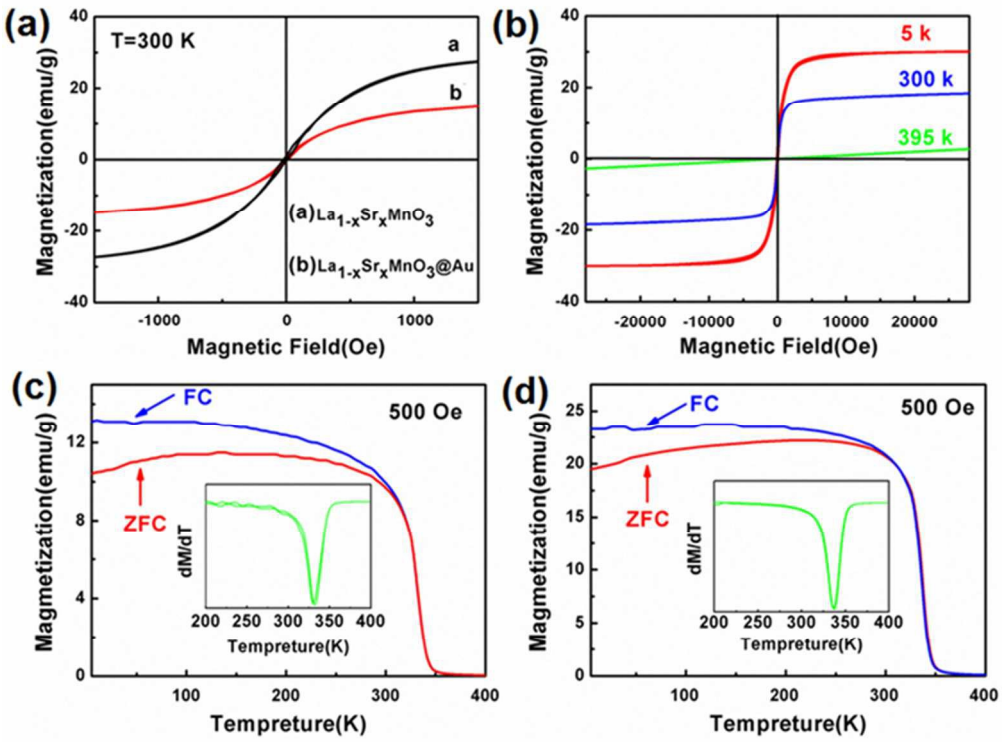

59x44mm (300 x 300 DPI)

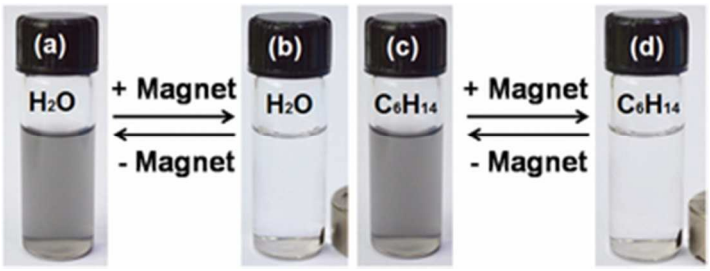

29x11mm (300 x 300 DPI)

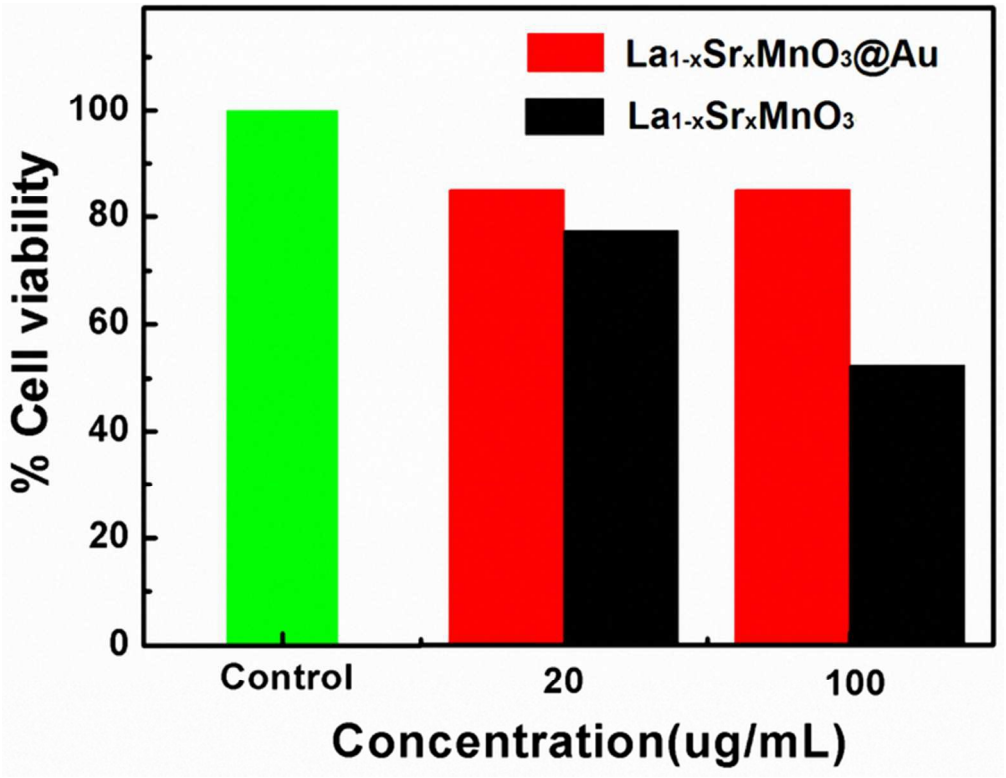

61x47mm (300 x 300 DPI)